Polymer 55 (2014) 4514–4520

Contents lists available at ScienceDirect

Polymer

journal homepage: www.elsevier.com/locate/polymer

Crystal structure and molecular packing of an asymmetric giant amphiphile constructed by one C_{60} and two POSSs

Ming-Champ Lin [a, b], Chih-Hao Hsu [a], Hao-Jan Sun [a], Chien-Lung Wang [a, c], Wen-Bin Zhang [a, d], Yiwen Li [a], Hsin-Lung Chen [b], Stephen Z. D. Cheng [a, *]

[a] Department of Polymer Science, College of Polymer Science and Polymer Engineering, The University of Akron, Akron, OH 44325-3909, USA
[b] Department of Chemical Engineering and Frontier Center of Fundamental and Applied Sciences of Matters, National Tsing Hua University, Hsin-Chu 30013, Taiwan
[c] Department of Applied Chemistry, National Chiao Tung University, 1001 Ta Hsueh Road, Hsin-Chu 30010, Taiwan
[d] Department of Polymer Science and Engineering, College of Chemistry and Molecular Engineering, Center for Soft Matter Science and Engineering, Peking University, Beijing 100871, China

ARTICLE INFO

Article history:
Received 8 May 2014
Received in revised form
1 July 2014
Accepted 7 July 2014
Available online 15 July 2014

Keywords:
Polyhedral oligomeric silsesquioxane
Fullerene
Amphiphile

ABSTRACT

Based on our recent understanding and development of functionalized molecular nanoparticles (MNPs) as building blocks for constructing various giant molecules, we report our efforts on design and synthesis of an asymmetric giant amphiphile, diBPOSS–C_{60}, composed of one [60]fullerene (C_{60}) covalently linked with two isobutyl-functionalized polyhedral oligomeric silsesquioxane (BPOSS) MNPs. Its crystal structure and molecular packing were investigated. The compositional asymmetry between C_{60} and BPOSS led to a "sandwich-layered" molecular packing scheme, where a single layer of C_{60} is sandwiched between double BPOSS layers: a so-called "one-and-half-layered" structure. Within these layers, the molecules further organized into crystalline arrays. Interestingly, this compound can be viewed as size amplification of a class of atomically thin, two-dimensional layered transition metal dichalcogenides with the "one-and-half-layered" structure.

1. Introduction

Recently, the design and synthesis of giant molecules based on "nano-atoms" have attracted significant attention for engineering structures at the length scales of sub-10 nm and controlling their macroscopic properties [1–4]. "Nano-atoms" are defined to consist of shape- and volume-persistent molecular nanoparticles (MNPs) with precisely defined chemical structures and surface functionalities. These "nano-atoms" act as building blocks for constructing precisely defined giant molecules which comprise many different types such as giant amphiphiles, giant polyhedra, giant surfactants, and others [3]. Among them, we especially focus on giant amphiphiles built up by covalently-linked MNPs with distinct shapes and interactions.

A number of MNPs with distinct shape and symmetry [5,6], size, chemical constitution (organic vs. inorganic) [7,8], and surface functionality [9,10] have been developed [11,12]. Among them, the most popular MNPs for constructing giant amphiphiles are perhaps polyhedral oligomeric silsesquioxanes (POSS) and [60]fullerene (C_{60}). They have comparable sizes of about 1 nm in diameter [13–19]. POSS is an inorganic molecule with a cubic-shaped cage composed of silicon–oxygen components. Within this family, the T_8 cage is the most common one, prepared by condensation of a silane/silanol precursor. Many POSS derivatives are available with different side groups, such as isopropyl, isooctyl, cyclopentyl, carboxylic acids, perfluorinated alkyl, and others, to tune the overall molecular sizes, surface chemistries and physical properties of POSS [20]. On the other hand, as a carbon allotrope, C_{60}, also known as a buckyball, is the smallest stable fullerene. It consists solely of carbon atoms arranged in five- and six-membered rings with a spherical shape and I_h symmetry, and it is also the most abundant one in the fullerene family [21]. Combining different numbers of POSS and C_{60} following a specifically designed molecular geometry is a straightforward pathway to build giant amphiphiles.

Previously, we have reported a symmetric giant amphiphile, BPOSS–C_{60}, constituted by a covalently linked POSS cage (with hydrophobic isobutyl surface groups, BPOSS) and spherical C_{60}. It is viewed to be a "dumbbell-like" shape (with similar sizes). Nanophase segregation with alternating "double-layered" structure of POSS and C_{60} was reported in the crystals [15]. In this "double-

* Corresponding author. Tel.: +1 44325 3909.
E-mail address: scheng@uakron.edu (S.Z.D. Cheng).

http://dx.doi.org/10.1016/j.polymer.2014.07.008
0032-3861/

layered" structure, the molecules assemble themselves into an alternating C_{60}-to-C_{60} and BPOSS-to-BPOSS configuration. Interestingly enough, depending on the ordering sequence of MNPs within each layer, the solid state structures exhibited polymorphism with two distinct crystal structures: orthorhombic and hexagonal packing schemes. Based on the crystal packing structure and density difference, the hexagonal lattice was identified to be the thermodynamically stable phase. Another "dumbbell-like" giant amphiphile was built up using solely POSS cages as building blocks. Thiol-ene "click" chemistry was used to break the chemical symmetry and introduce amphiphilicity [16]. The resulting giant molecule contains one POSS with hydrophobic isobutyl surface groups (BPOSS) and another with hydrophilic carboxylic surface groups (APOSS). The molecules self-assemble into an alternating "double-layered" structure that further organizes into a three-dimensional (3D) crystalline orthorhombic lattice [16].

The "double-layered" structures found in BPOSS–C_{60} and APOSS-BPOSS systems are likely attributed to the comparable sizes of the two MNPs as well as the immiscible or amphiphilic compositions on their surfaces. It is intriguing how symmetry breaking in this system such as relevant geometric variation and unbalanced number/composition affects their hierarchical structure formation and packing. Hence, we design a molecule that is composed of one C_{60} connected with two BPOSS MNPs (diBPOSS–C_{60}, Scheme 1). Since two BPOSS groups are covalently tethered onto one C_{60}, the overall symmetry of the molecule is reduced from I_h to C_{2v} [22,23].

An interesting aspect of this research in diBPOSS–C_{60} is how the compound arranges itself into the layered structure since the number of BPOSS and C_{60} MNPs in each molecule is now asymmetric. Analogues of this giant amphiphile in small molecules can be found in atomically thin, two-dimensional (2D) layered transition metal dichalcogenides (TMDCs) [24–26]. This class of materials exhibits electronic and optoelectronic properties superior to those of graphene as semiconductors and nano-scale coatings because of its tuneable band-gaps [27]. All of these of TMDCs, such as MoS_2 and WSe_2 (denoted as MX_2), possess a structure consisting of repetition of X-M-X "sandwich-layers" along the layer normal direction. The top and bottom layers are of chalcogenide atoms (X), arranged in hexagonal close packing symmetry, and one transition metal atom (M) layer is located in between those two chalcogenide atomic layers. In unifying with the concept of "double-layered" structures in BPOSS–C_{60} and APOSS–BPOSS systems, this type of molecular packing scheme should be a "one-and-half-sandwich-layered" structure. The fabrication of a mono-MX_2 layer is possible since the atoms within an individual "one-and-half-sandwich-layer" are held by strong covalent bonds, while only weak van der Waals interactions exist between the neighboring layers, enabling exfoliation to form single "one-and-half-sandwich-layered" sheets.

It is evident that the asymmetric giant amphiphile, diBPOSS–C_{60} could be viewed as a size-amplified analog of this MX_2 class of TMDC materials. The "one-and-half-sandwich-layered" structure resulting from specific interactions between transition metal atoms and chalcogenide atoms can be conceptually translated into the MNPs in diBPOSS–C_{60}. In this paper, we report our findings on the molecular design and crystal structure of diBPOSS–C_{60}. Indeed the "one-and-half-sandwich-layered" structure in this giant amphiphile can be experimentally verified: spherical C_{60}s form an interdigitated single layer that is sandwiched between two BPOSS layers. Such a layered structure consisting of the alternating conductive C_{60} layers and insulating BPOSS layers provides promising potential in practical applications of nano-capacitor [28]. Different from the previously reported BPOSS–C_{60} system, an asymmetric diBPOSS–C_{60} disclosed here shows two distinct layer thicknesses of BPOSS and C_{60}. This may provide significant insights into the strategy for controlling the thickness of conducting and insulating layers by utilizing different size or composition of MNPs, leading to the interesting electrical characteristics of nano-capacitors.

2. Experimental

2.1. Chemicals and solvents

PSS-(3-Hydroxypropyl)-heptaisobutyl (BPOSS–OH), toluene (anhydrous, 99.8%), iodine (≥99.8%), and 1,8-diazabicyclo[5.4.0]

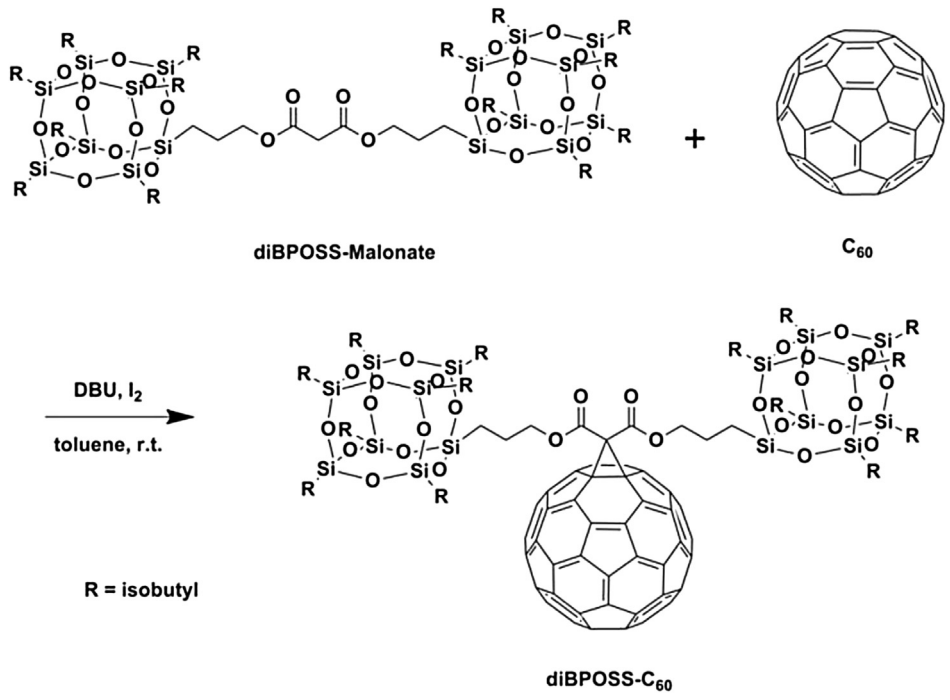

Scheme 1. Synthetic route to diBPOSS–C_{60}, where DBU stands for 1,8-diazabicyclo (5.4.0)undec-7-ene.

undec-7-ene (DBU, ≥99.8%) were purchased from Sigma–Aldrich and used as received without further purification. CH_2Cl_2 was purchased from Sigma–Aldrich and used after dried over CaH_2. [60] Fullerene (C_{60}, 99.9%) was purchased from MTR Ltd. and used as received.

2.2. Synthesis of diBPOSS–malonate

The diBPOSS–malonate was synthesized by the standard esterification protocol. In a 100 mL round-bottom flask, PSS-(3-Hydroxypropyl)-heptaisobutyl substituted (BPOSS–OH) (1.5 g, 1.71 mmol, 2.1 equiv) and N,N-Diisopropylethylamine (DIPEA) (0.21 g, 1.63 mmol, 2 equiv) were added followed by dissolving it in 20 mL of freshly dried CH_2Cl_2. This flask was then cooled in an ice water bath. Malonyl dichloride (0.115 g, 0.816 mmol, 1 equiv) was instilled dropwise into the flask via syringe after all of solids dissolved by stirring. This mixture was then kept being stirred at room temperature for 24 h. After that, the reaction solution was washed by NaCl saturated solution for three times and then evaporated under vacuum. The residue was purified by flash column chromatography on the silica gel with CH_2Cl_2/hexanes (v/v = 1/1) as eluent to afford the product. Yield: 80%. ^{1}H NMR (500 MHz, $CDCl_3$, cf. Fig. S1 in the Supporting Information, SI): δ (ppm) 4.11 (t, J = 10 Hz, 4H), 3.83 (s, 2H), 1.86 (m, 14H), 1.75 (m, 4H), 0.97 (m, 84H), 0.61 (m, 32H). ^{13}C NMR (125 MHz, $CDCl_3$, cf. Fig. S2): δ (ppm) 166.6, 67.4, 41.5, 29.7, 25.7, 25.7, 23.9, 23.8, 22.5, 22.4, 22.0, 8.2. Mass spectrum (ESI), cf. Fig. S3: calcd. monoisotopic mass for $C_{65}H_{140}NaO_{28}Si$ = 1839.6 Da; found: m/z = 1839.7 Da (100%) $[M\cdot Na]^+$.

2.3. Characterization of diBPOSS–malonate

All NMR experiment were performed in $CDCl_3$ (Aldrich, 99.8% D) on a Varian Mercury 500 NMR spectrometer. The ^{1}H NMR spectrum was referenced to the residual proton impurities in $CDCl_3$ at δ 7.27 ppm, and the ^{13}C NMR spectra were referenced to $^{13}CDCl_3$ at δ 77.00 ppm. In the ^{1}H NMR spectrum (Fig. S1), the appearance of a triplet at δ 4.11 ppm is characteristic of the methylene protons adjacent to the ester bond. In the ^{13}C NMR spectrum (Fig. S2), the sp^3 carbons of isobutyl groups on the POSS cage are evident at δ 25.7, 23.8 and 22.4 ppm. The mass spectrum was conducted on a HCT Ultra II quadrupole ion trap mass spectrometer (Bruker Daltonics, Billerica, MA) equipped with an electropray ionization (ESI) source. The sample solution was prepared in MeOH/$CHCl_3$ (1:3) at the concentration of 0.01 mg/mL with 1% NaTFA (1 mg/mL), and injected into the instrument at a flow rate of 180 μL/min. The nebulizer gas pressure was set at 10 psi, and the drying gas flow rate at 8 L/min, and temperature at 300 °C. The ESI mass spectrum (Fig. S3) revealed a m/z of 1839.7 Da, which matches well with the calculated 1839.6 Da for $C_{65}H_{140}NaO_{28}Si_{16}$ $[M\cdot Na]^+$.

2.4. Synthesis of diBPOSS–C_{60}

To a solution of C_{60} (100 mg, 0.11 mmol), bis(3-(heptaisobutylPOSS)propyl) malonate (180 mg, 0.10 mmol), and iodine (30 mg, 0.12 mmol) in 250 mL of toluene, DBU (35 μL, 0.23 mmol) was added. The mixture was stirred at room temperature for 12 h. After that, the solution was washed with H_2O (100 mL) and brine (100 mL). The organic phase was dried over $MgSO_4$ and then concentrated to give crude product. After column chromatography with silica gel using hexane/EA (v/v = 60/1) as eluent, diBPOSS–C_{60} was obtained as a dark brown powder (114 mg). Yield: 45%. ^{1}H NMR (300 MHz, $CDCl_3$, cf. Fig. S4): δ (ppm) 4.48 (t, J = 7 Hz, 4H), 2.0–1.84 (m, 18H), 0.96 (d, J = 7 Hz, 84H), 0.75 (m, 4H), 0.61 (d, J = 7 Hz, 28H). ^{13}C NMR (75 MHz, $CDCl_3$, cf. Fig. S5): δ(ppm) 163.5, 145.3, 145.1, 145.0, 145.0, 144.7, 144.6, 144.5, 144.5, 143.7, 142.9, 142.8, 142.8, 142.0, 141.8, 140.8, 138.8, 109.9, 71.5, 69.0, 29.5, 25.5, 25.5, 23.8, 23.7, 22.3, 22.3, 22.0, 8.3. FT-IR (KBr) ν(cm^{-1}), cf. Fig. S6: 1749 (C=O), 1266 (Si–C), 1230 (C–O),1105 (Si–O), 527 (C–C in C_{60}). Mass spectrum (MALDI–TOF), cf. Fig. S7: calcd. monoisotopic mass for $C_{125}H_{138}NaO_{28}Si$ = 2557.56 Da; found: m/z = 2557.89 Da (100%) $[M\cdot Na]^+$.

2.5. Characterization of diBPOSS–C_{60}

All NMR experiments were performed in $CDCl_3$ (Aldrich, 99.8% D) on a Varian Mercury 300 NMR spectrometer. The ^{1}H NMR spectra were referenced to the residual proton impurities in $CDCl_3$ at δ 7.27 ppm. The ^{13}C NMR spectra were referenced to $^{13}CDCl_3$ at δ 77.00 ppm. In the ^{1}H NMR spectrum (Fig. S4), the appearance of a triplet at δ 4.48 ppm is characteristic of the methylene protons adjacent to the ester bond. In the ^{13}C NMR spectrum (Fig. S5), the sp^2 carbons on C_{60} can be clearly seen at δ 138.8–145.3 ppm and the sp^3 carbons of isobutyl groups on the POSS cage are evident at δ 25.5, 23.7 and 22.3 ppm. The success in the cyclopropanation of the C_{60} is supported by the observation of the characteristic sp^3 carbon of the cyclopropyl unit, which is at δ 71.5 ppm. Infrared spectra were recorded on an Excalibur Series FT-IR spectrometer (DIGILAB, Randolph, MA) by dropping the diBPOSS–C_{60} solution on KBr plates with subsequent drying. The data were processed using Win-IR software. Matrix-assisted laser desorption/ionization time-of-flight (MALDI–TOF) mass spectra were recorded on a Bruker Ultraflex III TOF/TOF mass spectrometer (Bruker Daltonics, Billerica, MA), equipped with a Nd:YAG laser emitting at a wavelength of 355 nm with trans-2-[3-(4-tertbutylphenyl)-2-methyl-2-propenylidene]malononitrile (DCTB, Aldrich, >99%) as the matrix in $CHCl_3$ at a concentration of 20 mg/mL. The MALDI–TOF mass spectrum (Fig. S7) revealed an m/z of 2557.9, which matches well with the calculated 2557.6 Da for $C_{125}H_{138}NaO_{28}Si_{16}$. The thermogravimetric measurements were conducted on a TA TGA Q500 instrument at a scan rate of 10 °C/min under nitrogen. Thermal gravimetric analysis (Fig. S8) shows good thermal stability for diBPOSS–C_{60} with a 1% weight loss at a temperature of 298 °C.

2.6. Differential scanning calorimetry (DSC)

DSC experiments were carried out on a Perkin–Elmer PYRIS Diamond with an Intracooler 2P cooling system to study the crystallization and melting behavior of diBPOSS–C_{60}. Samples of ca. 3 mg were encapsulated in aluminum pans. The calibration was performed with indium and hexatricontane, and all tests were run using ultrapure nitrogen as purge gas. In the standard DSC experiment, the sample was first heated to 240 °C (a temperature ca. 40 °C higher than the melting point of diBPOSS–C_{60} crystals) and kept at that temperature for 15 min to erase previous thermal history. Then, a cooling scan at 10 °C/min was conducted down to 0 °C, followed by a subsequent heating run performed also at 10 °C/min.

2.7. Single crystal specimen preparation

The single crystals for electron microscopy experiments were prepared by casting a drop of diBPOSS–C_{60} solution in chloroform (0.2 mg/mL) onto a carbon-coated glass slide where the solution quickly spread out to generate a film at the carbon–air interface. After solvent evaporation, the film was thermally annealed at 240 °C on a hot stage under nitrogen for 15 min, followed by rapid cooling to a prescribed temperature for crystallization till saturation. After that, a thin film containing single crystal domains was obtained.

2.8. Transmission electron microscopy (TEM)

For transmission electron microscopy (TEM, Philips Tecnai 12 at an accelerating voltage of 120 kV) experiments, one drop of 25% poly(acrylic acid) (PAA) aqueous solution was placed on the surface of the film containing single crystals and was allowed to dry completely. The dried, hardened PAA droplet was then removed by a razor blade along with the sample film and the carbon film underneath. Then the droplet was transferred onto a water surface with PAA side touching the water. After a few minutes, the PAA dissolved and the thin film floated on the water surface. Clean TEM copper grids (400 mesh, SPI) were then used to pick up the film. Before TEM observation, the samples were put into a vacuum oven for 12 h to remove the residual solvent and moisture. The grids were then subjected to TEM experiments for bright field images and selective area electron diffraction (SAED) patterns. The *d*-spacings of SAED patterns were calibrated using a TlCl standard.

2.9. Density measurement

A small amount of crystals (~0.5 mg) was collected for density measurement. The sample was placed in a vial with water followed by ultrasonication to remove the air bubbles embedded within the sample. After that, the sample sank to the bottom of the vial, indicating that the density of the sample was higher than water. Potassium iodide (KI) was then added into the solution stepwise 0.1 g at a time to gradually increase the solution density at an interval of at least 20 min to ensure equilibrium within the solution. When the sample started to suspend in the middle of the solution, the density of the sample was deemed identical to that of the solution, which was determined with a volumetric flask.

2.10. Molecular simulation

Molecular modeling and diffraction pattern simulations of crystal structures were conducted on the Accelrys Cerius^2 software package (version 4.6). The lowest energy conformation of a diBPOSS–C_{60} in vacuum was chosen as the starting conformation. Lattice parameters used to build the unit cell were determined by the experimental crystallographic data extracted from SAED patterns. The final positions of atoms in the unit cell were judged by the result of energy minimization and comparing the relative intensities, related to the structure factor, between calculated ED patterns and the experimentally observed patterns.

2.11. Wide-angle X-ray diffraction (WAXD)

The temperature-dependent WAXD measurements were performed at station BL01C2 at the National Synchrotron Radiation Research Center, Taiwan, using an imaging plate as the detector. The X-ray beam with the wavelength of 0.954 Å was collimated into the beam size of 0.5 mm × 3 mm by two slits separated by 1.1 mm with a sample-to-detector distance of 420 mm. The beam center and the angular scale were calibrated using silver behenate, silicon, sodalite, and high-density polyethylene. The intensity was plotted against scattering angle (2θ), where the 2θ presented in this work was converted from $\lambda = 0.954$ Å to $\lambda = 1.54$ Å (as the conventional X-ray source given by CuK_α).

3. Results and discussion

The chemical structures and the synthetic route are presented in Scheme 1. The diBPOSS–C_{60} was synthesized in one step by coupling C_{60} and diBPOSS–malonate via the Bingel reaction in toluene [29]. The synthesized diBPOSS–C_{60} was fully characterized by nuclear magnetic resonance (^{1}H NMR, ^{13}C NMR), FT-IR, and MALDI–TOF mass spectroscopy (see Figs. S1–S7 in the SI). All of these results confirm the success of the Bingel reaction and the formation of the proposed chemical structure.

The phase behavior of diBPOSS–C_{60} was first investigated utilizing DSC. Fig. 1 shows the DSC diagrams of both cooling from the melt (black) and subsequent heating at a rate of 10 °C/min (red). Upon cooling from the melt, no distinct exothermic process is observed, indicating that the crystallization of diBPOSS–C_{60} does not take place at this cooling rate. A similar result was observed when the system was subjected to a lower cooling rate (5 °C/min) (the result is not shown). During the subsequent heating (red), a sudden step change of the heat capacity was recognized as the glass transition temperature at $T_g = 57$ °C. As the temperature further increased, an exothermic process appeared at around 111.7 °C, followed by a multiple melting process between 165 °C and 200 °C. These results reveal that upon cooling diBPOSS–C_{60} does not have enough time to develop crystals (only form a few nuclei). Only during the subsequent heating at 10 °C/min, the crystallization can be induced as evidenced by a large exotherm [30,31]. The above thermal behavior (the appearance of an exothermic process followed by a multiple melting process in the heating scan) is unaffected by use of different scan rates (ranging from 5 to 20 °C/min, see Fig. S9 in the SI), although the areas of the multiple melting processes are not the same. The multiple endothermic processes observed between 165 °C and 200 °C may be attributed to either the melting of different crystal forms (polymorphs with different melting temperatures) or of a single crystal form with distinct metastabilities (largely due to different crystallite sizes) [31]. These two possible interpretations were assessed using temperature-dependent WAXD experiments.

Fig. 2 shows a set of 1D WAXD powder patterns collected by stepwise heating at each of the indicated temperatures after the sample was first cooled from 240 °C to 0 °C at a rate of 10 °C/min. At 30 °C, three correlation-hole halos can be identified at around $2\theta \sim 2.8°$, 9°, and 19°, indicating that three short-range ordered correlation distances exist in diBPOSS–C_{60}. The exact physical meanings of these three distances can be understood after the corresponding crystal structure is determined (see below). Furthermore, this WAXD pattern at 30 °C is very similar to that recorded at 200 °C in the melt, indicating that no substantial crystals are formed during cooling at 10 °C/min. With increasing

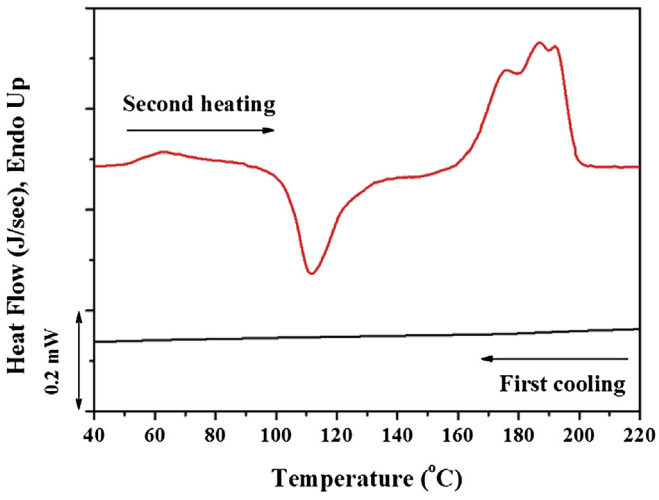

Fig. 1. DSC cooling scan (at 10 °C/min) from the melt (black) and the subsequent heating scan (at 10 °C/min) of diBPOSS–C_{60} (red).

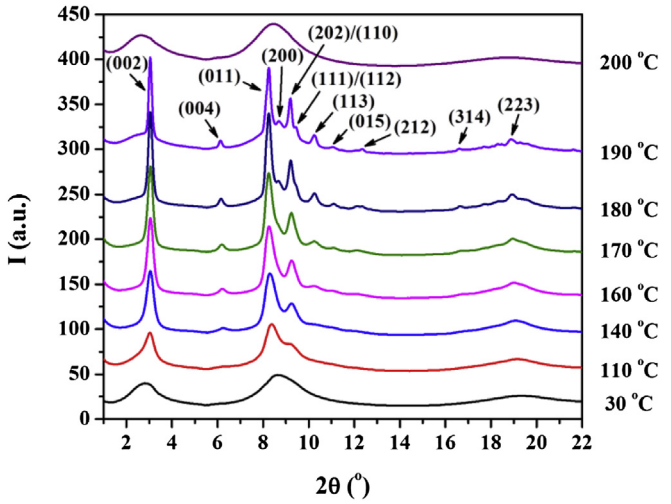

Fig. 2. Temperature-dependent WAXD powder patterns of diBPOSS–C_{60} upon stepwise heating from 30 °C to 200 °C. The sample was first cooled from 240 °C to 0 °C at 10 °C/min (this cooling history was identical to that employed for DSC measurement shown in Fig. 1) before the data acquisition.

temperature, the diffraction peaks start to appear at 110 °C. This structural development echoes the exothermic process observed in DSC diagram in Fig. 1. The diffraction peaks are continuously sharpened as their intensities are enhanced until the temperature reaches 190 °C. The fact that no diffraction peak positions exhibit sudden changes during the heating until the complete crystal melting, indicating that only one crystal form exists in diBPOSS–C_{60}. Therefore, the multiple melting peaks in the DSC diagram in Fig. 1 must be due to the crystals having various sizes formed under thermal annealing and thus, with different metastabilities [31]. As the temperature raises to over 200 °C, all the diffraction peaks vanish and only three correlation-hole halos remain, revealing that the system reaches the isotropic melt. The WAXD patterns and DSC diagrams provide the information of phase behavior and structural development. However, the detailed crystal lattice, unit cell dimensions, and space group need to be determined based on the SAED results with diBPOSS–C_{60} single crystals.

The upper right inset in Fig. 3a presents a bright-field TEM image of a flat-on single crystal of diBPOSS–C_{60} isothermally crystallized at 140 °C in the thin film melt. The corresponding SAED pattern with the [001] zone shows an orthogonal a^*- and b^*-axes, indicating a 2D rectangular reciprocal lattice in the a^*b^* plane. Moreover, the odd (h00) and (0k0) diffractions are extinct except for a pair of the weak (010) diffractions along the b^*-axis (Fig. 3a). The dimensions of the projected 2D rectangular lattice are thus determined to be $a = 2.03$ nm, $b = 1.06$ nm, and $\gamma = 90°$. Single crystals of diBPOSS–C_{60} with the edge-on arrangement can also be observed as shown in the upper right inset of Fig. 3b. The corresponding SAED pattern of the [100] zone shows that the c^*-axis of the diBPOSS–C_{60} crystal is also perpendicular to the b^*-axis, revealing the angle of $\alpha = 90°$. Moreover, the odd (00l) diffractions were again found to be extinct and the d-spacing of the (002) plane was measured to be 2.83 nm and thus, the c-axis dimension was deduced to be 5.66 nm. Identical SAED results were obtained for diBPOSS–C_{60} crystallized at other temperatures ranging from 90 to 142.5 °C. After cell parameter refinement, the unit cell based on the SAED and WAXD results was determined to be orthorhombic with the lattice parameters of $a = 2.03$ nm, $b = 1.06$ nm, $c = 5.66$ nm, and $\alpha = \beta = \gamma = 90°$. The calculated crystallographic density was 1.38 g/cm^3 based on four diBPOSS–C_{60} molecules within each unit cell ($Z = 4$), and it agrees well with the experimental value of 1.36 g/cm^3 obtained from the density measurement. The space group was identified to be Pnnm (No. 58) based on the extinction rules observed in the SAED patterns as well as the molecular symmetry [22].

According to this crystal lattice and dimensions, we can assign the diffraction peaks (ranging from 1° to 22°) observed in the WAXD powder pattern of Fig. 2. All of the experimentally observed 2θ angle and d-spacings are in excellent agreement with the calculated ones as shown in Table S1 in the SI. In addition, two smeared correlation-hole halos seem to exist at ~9° and ~19°; they must be attributed to the amorphous (or molten) region with average inter- and intra-molecular distances between the MNPs (either between BPOSSs, C_{60}s, and/or BPOSS and C_{60}).

To unequivocally verify the crystal lattice and dimensions, we further investigated the detailed molecular packing of diBPOSS–C_{60} in the orthorhombic lattice. This was simulated via Accelrys Cerius^2 package manipulated by subjecting all molecules to an initial energy minimization using the universal force field.

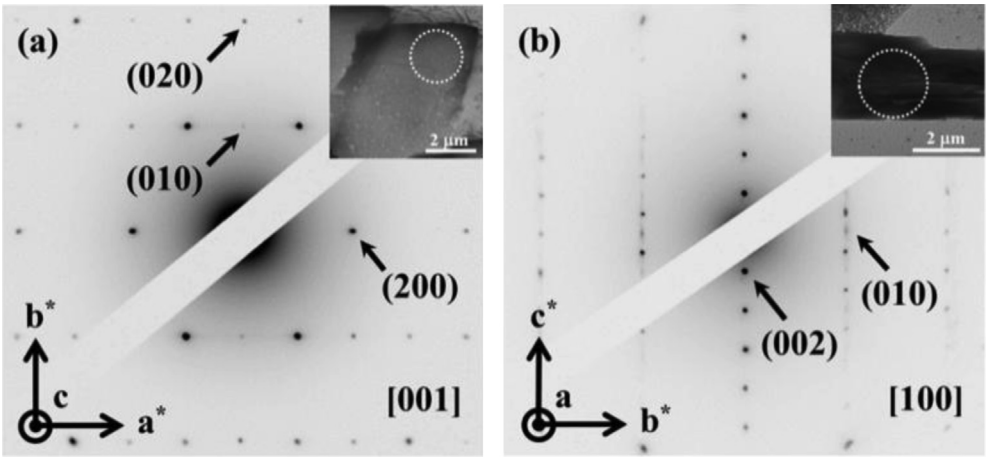

Fig. 3. (a) SAED pattern of the [001] zone obtained from the selected circular area marked in its upper right inset. The inset in (a) presents the TEM bright field image of a flat-on single crystal of diBPOSS–C_{60} after isothermal crystallization at 140 °C from the melt. (b) SAED pattern of the [100] zone obtained from the selected circular area marked in its upper right inset. The inset in (b) shows the TEM bright field image of a portion of bundle-like crystals, consisting of edge-on single crystals of diBPOSS–C_{60} subjecting to the same thermal treatment as (a). The scale bar shown in the inset of (a) and (b) represents 2 μm.

Fig. 4a–c shows three projections of this orthorhombic unit cell with the space group of *P*nnm along the [010], [100] and [001] directions, respectively. In this set of figures, totally sixteen diBPOSS–C_{60} molecules are included with a crystal dimension of 2*a*, 2*b* and 1*c*.

When viewed along the *b*-axis (i.e., the [010] zone) in the *ac*-plane, the "sandwich-layered" structure can be easily identified in Fig. 4a. It reveals that the C_{60}s interdigitate with each other to fill in the space as a separate layer, while two layers of BPOSSs are located at the top and bottom of this single C_{60} layer (the "one-and-half-sandwich-layered" structure). However, it should be noted that the BPOSS cages in the top layer are shifted *b*/2 along the *b*-axis as compared with that in the bottom layer, as can be clearly seen in Fig. 4b when viewed along the *a*-axis projection. That is, in the *bc*-plane the BPOSS cages in the top sandwich-layer are located in between, but not overlap, the BPOSS cages in the bottom sandwich-layer. Due to the 2_1/m symmetry operation along the *c*-axis, the molecular arrangement along the *c*-axis consists of two sets of BPOSS–C_{60}–BPOSS sandwich-layered structures. Fig. 4c shows the arrangement of the C_{60} and BPOSS projections in the *ab*-plane. The two BPOSS cages in each molecule are aligned along the *a*-axis and packed side-by-side with the neighboring molecules along the *b*-axis, generating a simple rectangular arrangement in the *ab*-plane. This arrangement leads to center-to-center distances between the underneath C_{60}s (those connected to the top BPOSS layer) of 2.03 nm along the *a*-axis and 1.06 nm along the *b*-axis, respectively. Every C_{60} connected to the bottom BPOSS layer sits in the cavity created by the four C_{60}s connected to the top BPOSS layer, which allows the bottom BPOSS layer to slide (*a* + *b*)/2 in the *ab*-plane with respect to the top BPOSS layer. The simulation of molecular packing after energy minimization shows the existence of diagonal glide planes perpendicular to both of the *a*- and *b*-axes, a mirror plane perpendicular to the *c*-axis, and two-fold screw axes along all three axes (cf. Fig. 4a–c) that are consistent with the symmetry of *P*nnm. The translational movements as a result of the glide plane operations gives rise to the extinction of odd (*h*00), (0*k*0), and (00*l*) diffractions observed in Fig. 3a and b. A weak reflection of the (010) observed in the SAED pattern (Fig. 3a and b) must indicate imperfect packing of C_{60}s along the *b*-axis, which is most likely attributed to the slow kinetics during crystal growth that led to packing defects in the C_{60} layer [32].

Based on the molecular packing scheme established in Fig. 4a–c, the computer-simulated ED patterns with the [001] and [100] zones were generated as shown in Fig. 4d and e, respectively. Quantitatively, these patterns agree well with the experimental SAED patterns in terms of the diffraction positions (cf. Fig. 3a and b); semi-quantitatively, the relative intensities of diffraction spots are also consistent with the experimental observation. Therefore, the molecular arrangement depicted in Fig. 4a–c represents an accurate description of the overall symmetry and molecular packing of diBPOSS–C_{60} in the orthorhombic lattice and verifies the previous structural determination.

Previously reported BPOSS–C_{60} dyad and APOSS-BPOSS molecules possess "double-layered" structures along the long-axis of the giant amphiphile (i.e., the layer normal direction). However, in the case of diBPOSS–C_{60}, the component imbalance brings further

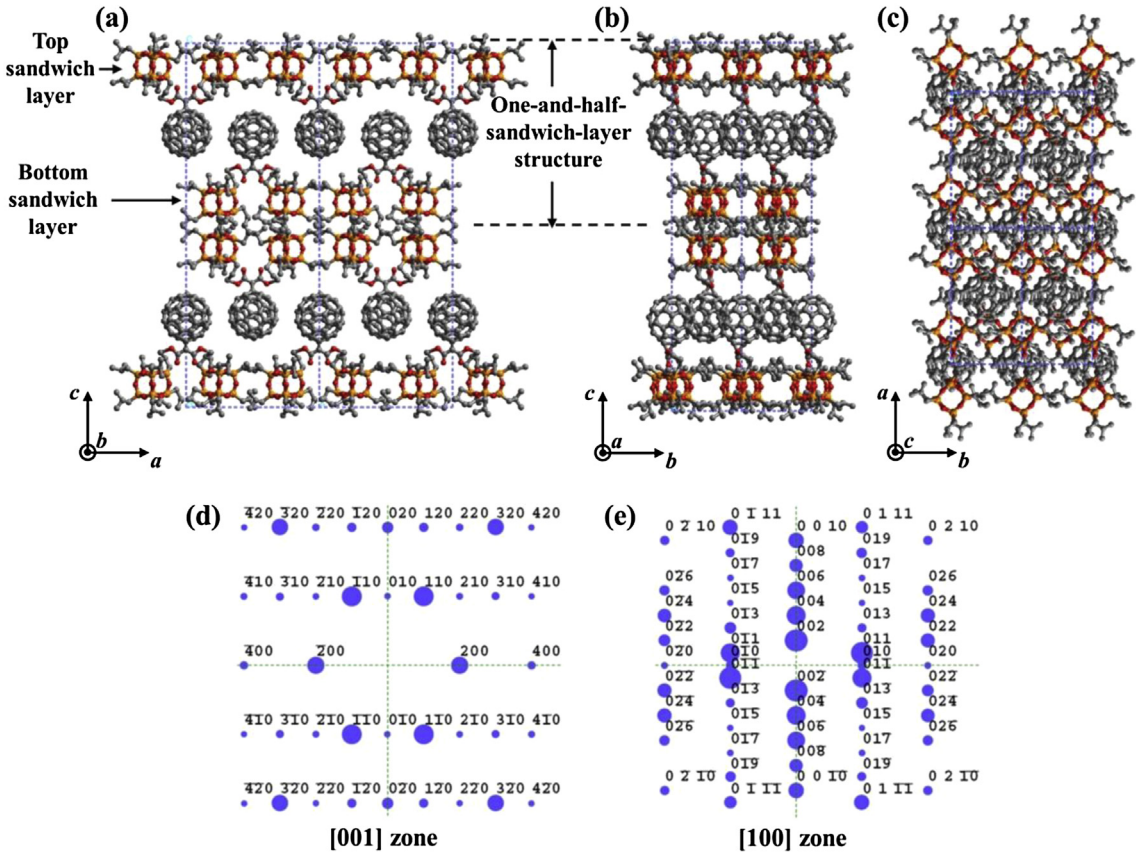

Fig. 4. Simulations of molecular packing in the orthorhombic crystal lattice with dimensions of 2*a*, 2*b*, and 1*c* on (a) the *ac*-plane when projected from the *b*-axis direction; (b) the *bc*-plane when projected from the *a*-axis direction; (c) the *ab*-plane when projected from the *c*-axis direction. The silver spheres represent C_{60}s while the orange-red cubes indicate BPOSSs. The computer-simulated ED patterns are along (d) the [001] zone; and (e) the [100] zone.

symmetry breaking on the overall molecular shape and leads to the formation of a "one-and-half-sandwich-layered" structure. The pristine C_{60} molecule intrinsically possesses I_h symmetry and is known to form a face-centered cubic plastic crystal [33,34]. By anchoring two BPOSS molecules, the rotational symmetry of the molecule is broken from nearly C_∞ symmetry of a spherical object (C_{60}) to C_{2v} symmetry (diBPOSS–C_{60}). Moreover, both the number and shape of BPOSS and C_{60} (with a ratio of 2:1) in each diBPOSS–C_{60} molecule are incommensurate in space, forcing the BPOSSs to adopt the head-to-head (and tail-to-tail) arrangement in which the C_{60}s being interdigitated with each other in the layered structure in order to achieve the most close packing density in the crystal. Hence, the layered structure formed in diBPOSS–C_{60} system is different from those commonly observed "double-layered" structures. Yet, we can clearly recognize that the crystal structure and molecular packing of diBPOSS–C_{60} exhibit size-amplified layer structures of MX_2 in 2D TMDCs. Currently, we are focusing on the study of electronic and optoelectronic properties of diBPOSS–C_{60}.

4. Conclusion

In summary, an asymmetric giant amphiphile diBPOSS–C_{60} has been designed and synthesized. Crystals of this giant molecule were grown in the melt. The diBPOSS–C_{60} crystal lattice and dimensions have been determined to be an orthorhombic unit cell with $a = 2.03$ nm, $b = 1.06$ nm, $c = 5.66$ nm, and $\alpha = \beta = \gamma = 90^\circ$. The molecular packing has also been illustrated via computer simulation. The results reveal a "one-and-half-sandwich-layered" structure along the *c*-axis, which consists of one layer of interdigitated C_{60}s sandwiched between two layers of BPOSS cages. This packing scheme repeats itself along the *c*-axis to form a 3D orthorhombic lattice with the symmetry group of *P*nnm. Such a layer structure arises from symmetry breaking in molecular shape and component imbalance as compared to the previously studied "dumbbell-like" giant amphiphiles. This investigation provides a model system of precisely defined giant molecules, composed of covalently linked "nano-atoms", which represents size amplification of the layered structures of atomically 2D MX_2 class in TMDC materials.

Acknowledgment

The financial support from the Study Abroad Program for Graduate Students (the "Thousand-Mile Horse" Program) sponsored by the National Science Council, Taiwan, for MCL to conduct this research at The University of Akron is gratefully acknowledged. At The University of Akron, this work was supported by National Science Foundation (DMR-0906898 and DMR-1408872). SZDC and WBZ acknowledge support from The Joint-Hope Education Foundation. The assistance of Wen-Bin Su and Chien-Liang Liu when carrying out the WAXD experiments is highly appreciated. We also thank the National Synchrotron Radiation Research Center at Taiwan for supporting the X-ray powder diffraction experiments at beamline 01C2.

Appendix A. Supplementary data

Supplementary data related to this article can be found at http://dx.doi.org/10.1016/j.polymer.2014.07.008.

References

[1] Roy X, Lee CH, Crowther AC, Schenck CL, Besara T, Lalancette RA, et al. Science 2013;341:157–60.
[2] Yu XF, Hsieh IF, Li YW, Dong XH, Liu C, Xin Y, et al. Proc Natl Acad Sci 2013;110:10078–83.
[3] Zhang WB, Yu XF, Wang CL, Sun HJ, Hsieh IF, Li YW, et al. Macromolecules 2014;47:1221–39.
[4] Cheng SZD. J Polym Sci B Polym Phys 2005;43:3361–4.
[5] Kitaev V. J Mater Chem 2008;18:4745–9.
[6] Jun YW, Seo JW, Oh SJ, Cheon J. Coord Chem Rev 2005;249:1766–75.
[7] Patil AJ, Mann S. J Mater Chem 2008;18:4605–15.
[8] Steinmetz NF, Bize A, Findlay KC, Lomonossoff GP, Manchester M, Evans DJ, et al. Adv Funct Mater 2008;18:3478–86.
[9] Zhang WB, Li YW, Li XP, Dong XH, Yu XF, Wang CL, et al. Macromolecules 2011;44:2589–96.
[10] Yu XF, Zhong S, Li XP, Tu YF, Yang SG, Van Horn RM, et al. J Am Chem Soc 2010;132:16741–4.
[11] Glotzer SC, Solomon MJ. Nat Mater 2007;6:557–62.
[12] Reynhout IC, Cornelissen JJLM, Nolte RJM. Acc Chem Res 2009;42:681–92.
[13] Yu XF, Zhang WB, Yue K, Li XP, Liu H, Xin Y, et al. J Am Chem Soc 2012;134:7780–7.
[14] Dong XH, Zhang WB, Li YW, Huang MJ, Zhang SO, Quirk RP, et al. Polym Chem 2012;3:124–34.
[15] Sun HJ, Tu YF, Wang CL, Van Horn RM, Tsai CC, Graham MJ, et al. J Mater Chem 2011;21:14240–7.
[16] Li YW, Zhang WB, Hsieh IF, Zhang GL, Cao Y, Li XP, et al. J Am Chem Soc 2011;133:10712–5.
[17] Cordes DB, Lickiss PD, Rataboul F. Chem Rev 2010;110:2081–173.
[18] Zhang WB, Tu YF, Ranjan R, Van Horn RM, Leng SW, Wang J, et al. Macromolecules 2008;41:515–7.
[19] Prassides K, Alloul H. Fullerene-based materials: structures and properties. Berlin, Heidelberg New York: Springer; 2004.
[20] Baney RH, Itoh M, Sakakibara A, Suzuki T. Chem Rev 1995;95:1409–30.
[21] Kroto HW, Heath JR, Obrien SC, Curl RF, Smalley RE. Nature 1985;318:162–3.
[22] Hahn T, editor. International tables for crystallography, vol. A. Dordrecht, Boston: Reidel Publishing Company; 1992.
[23] Clegg W. Crystal structure determination. Oxford, New York: Oxford University Press; 1998.
[24] Chhowalla M, Shin HS, Eda G, Li LJ, Loh KP, Zhang H. Nat Chem 2013;5:263–75.
[25] Ataca C, Sahin H, Ciraci S. J Phys Chem C 2012;116:8983–99.
[26] Wang QH, Kalantar-Zadeh K, Kis A, Coleman JN, Strano MS. Nat Nanotech 2012;7:699–712.
[27] Radisavljevic B, Radenovic A, Brivio J, Giacometti V, Kis A. Nat Nanotech 2011;6:147–50.
[28] Shi G, Hanlumyuang Y, Liu Z, Gong Y, Gao W, Li B, et al. Nano Lett 2014;14:1739–44.
[29] Bingel C. Chem Ber 1993;126:1957–9.
[30] Cheng SZD, Lotz B. Polymer 2005;46:8662–81.
[31] Cheng SZD. Phase transitions in polymers: the role of metastable states. Elsevier Science; 2008.
[32] Yase K, Ara-Kato N, Hanada T, Takiguchi H, Yoshida Y, Back G, et al. Thin Solid Films 1998;331:131–40.
[33] David WIF, Ibberson RM, Matthewman JC, Prassides K, Dennis TJS, Hare JP, et al. Nature 1991;353:147–9.
[34] Heiney PA, Fischer JE, McGhie AR, Romanow WJ, Denenstein AM, McCauley JP, et al. Phys Rev Lett 1991;66:2911–4.